

MgCr₂O₄-Modified CuO/Cu₂O for High-Temperature Thermochemical Energy Storage with High Redox Activity and Sintering Resistance

Jiali Deng, Changdong Gu, Haoran Xu, and Gang Xiao*



Cite This: *ACS Appl. Mater. Interfaces* 2022, 14, 43151–43162



Read Online

ACCESS |

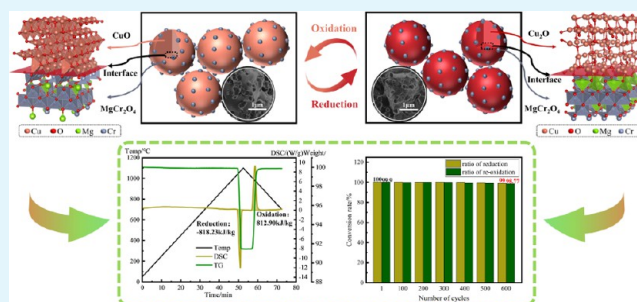
Metrics & More

Article Recommendations

Supporting Information

ABSTRACT: Metal oxides as high-temperature thermochemical energy storage systems with high energy density based on the gas–solid reaction are a critical demand for the future development of concentrated solar power plants. A copper-based system has high enthalpy change and low cost, but its serious sintering leads to poor reactivity. In this study, MgCr₂O₄ is decorated on the CuO/Cu₂O surface to effectively increase the sintering temperature and alleviate the sintering problem. The re-oxidation degree is increased from 46 to 99.9%, and the reaction time is shortened by 3.7 times. The thermochemical energy density of storage and release reach -818.23 and 812.90 kJ/kg, respectively. After 600 cycles, the oxidation activity remains 98.77%. Material characterization elucidates that nanosized MgCr₂O₄ is uniformly loaded on the surface of CuO/Cu₂O during the reversible reaction, and there is a strong interaction between metal oxides and prompter. Density functional theory (DFT) calculation further confirms that CuO/Cu₂O–MgCr₂O₄ has large binding energy and the formation energy of copper vacancy increases, which can effectively inhibit sintering. The modification mechanism of CuO/Cu₂O by MgCr₂O₄ is revealed, which can provide guidance for the reasonable design of thermochemical energy storage materials with sintering resistance and redox activity.

KEYWORDS: solar energy, thermochemical energy storage, sintering resistant, cycle stability, modification mechanism



1. INTRODUCTION

Concentrated solar power (CSP) plants equipped with an energy storage system are one of the most promising clean large-scale technologies that can provide cost-effective and dispatchable renewable power while addressing the challenge of intermittency.¹ Thermochemical energy storage (TCES), which allows higher operating temperature and higher storage density than the current commercial molten-salt storage systems, should be more suitable for the next-generation CSP plants to improve the thermodynamic efficiency of power generation.² The metal-oxide redox system is the most potential candidate for TCES based on solid–gas reversible reactions³ because of its better compatibility with CSP.^{4,5} Co₃O₄/CoO, Mn₂O₃/Mn₃O₄, and CuO/Cu₂O have been favored by researchers.^{3,6–9} The Co₃O₄/CoO redox couple has high enthalpy and excellent cycle stability in pure metal oxides, but Co is a scarce mineral resource and toxic.^{8,10–14} The Mn₂O₃/Mn₃O₄ system has poor reversibility, but its re-oxidation reaction kinetics and cycle stability can be effectively improved by doping with other elements (such as Si, Mg, Fe, etc.).^{15–19} However, its energy storage density is lower and a large hysteresis interval between oxidation and reduction leads to adverse effects on the exergetic efficiency of the energy storage process.²⁰ The CuO/Cu₂O system has higher reaction

enthalpy, lower cost, and smaller hysteresis temperature gaps,^{7,21} but sintering at high temperature leads to slow oxidation and short cycle life.^{3,8,22} If the existing problems can be solved by simple and cheap means while preserving the advantages of CuO/Cu₂O, the system is a very attractive choice.

The melting point of Cu₂O is about 1235 °C,⁷ which is only 135 °C above the maximum operating temperature of 1100 °C. It is close to the reduction temperature, and the grain is obviously sintered and grown,^{8,22} resulting in the serious deterioration of material performance. Researchers in the field currently focus on the resistance to sintering of CuO/Cu₂O by adjusting the oxygen concentration and adding other elements to form binary metal oxides. Deutsch et al. studied the redox characteristics of CuO/Cu₂O by changing the partial pressure of oxygen at 950 °C, and the results reflected that the

Received: May 28, 2022

Accepted: September 6, 2022

Published: September 19, 2022



maximum process temperature of the reduction reaction could be reduced by decreasing the oxygen partial pressure.²³ Jahromy et al. also described the impact of partial pressure and temperature on the oxidation reaction kinetics of Cu₂O to CuO.²¹ Since sintering increases exponentially with temperature, the decrease in the maximum reaction temperature can slow down sintering. However, such measures will increase system complexity and costs. Block et al. tested the reactivity of Cu-based composites with the addition of Co, Cr, Fe, and Mn, and the results showed that these binary oxide systems were reversible but lost part of the enthalpy of the reaction.²⁴ Scholars in other application areas related to alleviating sintering problems have reported the method of using a sintering inhibitor to improve sintering resistance. Imtiaz et al. used 70–90 wt % copper-based oxygen carriers with MgAl₂O₄ loadings as a sintering inhibitor and found that the sample covered with MgAl₂O₄ grains on the surface of the oxygen carrier has stability (25 cycles) and sintering resistance.²⁵ However, the MgAl₂O₄ grains are obviously agglomerated and have poor dispersion on the carrier. In previous work, we reported that the Al element helped to avoid CuO sintering and improve the re-oxidation rate. After 120 cycles, the oxidation degree of Cu–Al oxides maintained 81.1% of the initial capacity.²⁶ However, CuAl₂O₄ generated by the combination of Al₂O₃ and CuO consumes some CuO/Cu₂O, compromising the reaction performance. The structural design of their composites is slightly inadequate, which may lead to performance degradation after multiple cycles at high temperatures. In short, it is very necessary to develop a low-cost modification strategy that takes into account both sintering resistance and energy density.

In this paper, we designed a composite structure of Cu-based TCES materials that used a nanoprompter to minimize sintering without compromising the CuO/Cu₂O energy density. MgCr₂O₄ nanoparticles can be uniformly modified on the surface of CuO/Cu₂O in this method, which does not affect the reactivity of CuO/Cu₂O while maximizing the role of spatial confinement to alleviate sintering. Also, MgCr₂O₄-modified CuO/Cu₂O materials with high redox activity were synthesized by simple preparation methods. The structure, morphology, and chemical composition of the composites were characterized, and the interaction between MgCr₂O₄ and CuO/Cu₂O was analyzed to reveal the mechanism of sintering resistance and the improvement of reaction performance. Furthermore, combined with density functional theory (DFT) calculation, the strong binding of metal oxides with prompter and its influence on copper vacancy formation during the redox process were elucidated, which provided more in-depth insights for ameliorating sintering. This mechanism can offer ideas for the rational design of high-performance and long-life metal oxides with sintering resistance.

2. MATERIALS AND METHODS

2.1. Material Preparation. Integration of the sol–gel and high-temperature solid-phase methods was used to prepare MgCr₂O₄-modified CuO materials. The MgCr₂O₄ spinel structure prompter was synthesized by the sol–gel method in the following steps: Magnesium nitrate, chromium nitrate, and citric acid (CA) with a molar ratio of 1:2:3 were weighed and dissolved in an appropriate amount of deionized water and stirred at 70 °C for 3 h; then, ethylene glycol (EG) with a molar ratio of CA/EG = 3:2 was added and stirred at 90 °C for 2 h; subsequently, the gel was dried at 200 °C for 3 h and calcined at 450 °C for 4 h and 800 °C for 4 h in a muffle furnace with a heating rate of 10 °C/min. Finally, the as-prepared MgCr₂O₄ and

CuO powders were thoroughly mixed in a ball mill according to the corresponding mass fraction ratio and calcined at 900 °C for 4 h to obtain the modified composites. In this paper, MC-5, MC-10, MC-15, and MC-20 represent the samples with CuO- and MgCr₂O₄-doped mass percentages of 95:5, 90:10, 85:15, and 80:20 wt %, respectively.

2.2. Material Testing and Characterizations. The phase composition and crystal structures of the samples were collected by powder X-ray diffraction (XRD) patterns on an X'Pert Powder diffractometer equipped with Cu K α radiation source ($\lambda = 1.5406 \text{ \AA}$) operating at 40 kV and 40 mA. The scanning rate was 0.02°, and the most informative data was recorded in the range of 2θ of 10–80°. The morphology and microstructure of the product were investigated by field emission scanning electron microscopy–energy-dispersive spectroscopy (FESEM-EDS) on a SU-8010 microscope equipped with an Oxford X-max80 spectrometer. The redox activity and energy density were monitored by simultaneous thermal analysis (TGA/DSC3+) with heating in air at a flow rate of 50 mL/min. Also, the test temperature range was 50–1100–700 °C at a heating/cooling rate of 20 °C/min. The interaction of prompter and metal oxides was characterized by Fourier transform infrared (FTIR) spectra on a Thermo Scientific Nicolet iS20 spectrometer using KBr pellets in the range of 4000–400 cm⁻¹ with a resolution of 4 cm⁻¹. The analysis of surface chemistry of materials by X-ray photoelectron spectroscopy (XPS) was performed on a Thermo Scientific K-Alpha electron energy analyzer with monochromatic Al K α (1486.6 eV) radiation, which was operated at 15 kV. The binding energy (BE) value of C 1s at 284.8 eV was used to calibrate the peak positions of various elements. The surface areas were measured on an ASAP2460 automatic specific surface and micropore size analyzer using N₂ adsorption isotherms and calculated by the Brunauer–Emmett–Teller (BET) theory.

2.3. DFT Computation. All of the calculations were performed using periodic, spin-polarized density functional theory (DFT) as implemented in the Vienna ab initio simulation package (VASP)²⁷ using the generalized gradient approximation (GGA) with the Perdew–Burke–Ernzerhof (PBE) exchange–correlation function.²⁸ To describe the core–valence interaction, the projector-augmented wave (PAW) method was used.²⁹ For valence electrons, the plane-wave basis set was obtained with a kinetic energy cutoff of 500 eV. To accurately address the strong electron correlation effects in Cu and Cr, the DFT + *U* method was implemented.³⁰ We applied *U* = 7 eV to the Cu 3d³¹ and 3 eV for Cr 3d,³² respectively. For energy calculations, the convergence criterion of the total energy was set to 1.0 × 10⁻⁴ eV, and all of the atoms and geometries were optimized until the residual forces were less than 0.02 eV/Å. The Brillouin zone of the Monkhorst–Pack grid is set in Table S1. The lattice constants calculated by DFT are in good agreement with the experimental data with small deviations, as shown in Table S2. These results showed that the DFT calculation was reliable for geometric optimization. Because CuO(111), Cu₂O(111), and MgCr₂O₄(111)³³ are stable low-index surfaces, they were selected for this work. For the surface slab calculations, we adopted a slab/vacuum geometry composed of repeating slabs and vacuum layers. The detailed structural parameters of slab models are listed in Table S3. The surface model was further expanded by the supercell method into a p(2 × 2) surface unit cell. A vacuum thickness of 20 Å in the *z*-direction was placed to avoid spurious interactions between neighboring slabs.

3. RESULTS AND DISCUSSION

3.1. Thermochemical Energy Storage Performance.

The phase composition of the as-prepared composites is analyzed by XRD, as shown in Figure S1. The diffraction peaks of all samples could be indexed as CuO (ICDD-PDF No. 48-1548, C2/c monoclinic space group) and MgCr₂O₄ (ICDD-PDF No. 10-0351, *Fd* $\bar{3}m$ cubic space group). The diffraction peaks were intense, implying good crystallinity. The composites with different doping amounts did not form new phases, indicating that the prompter existed alone without

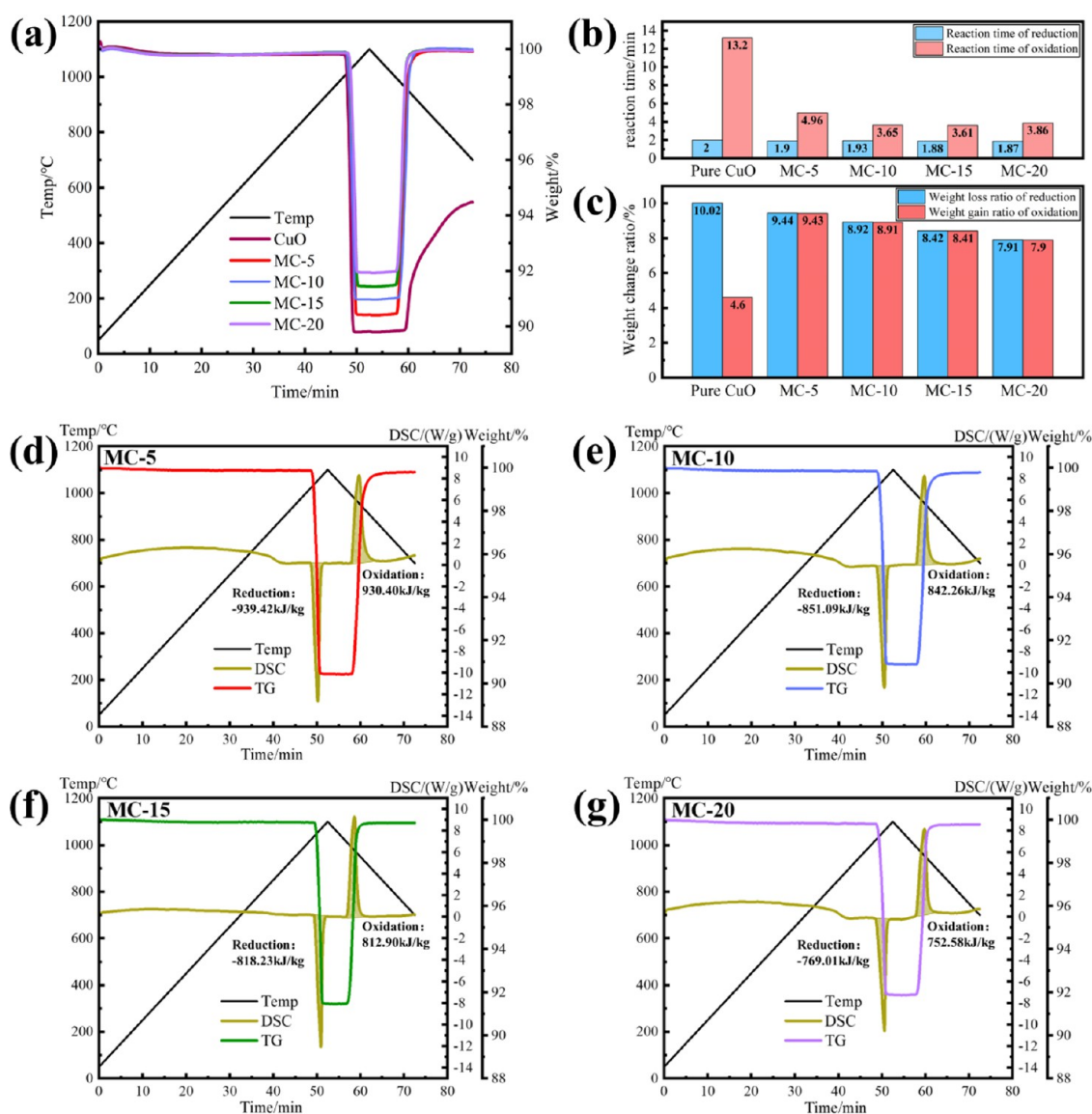


Figure 1. Redox reaction characteristics of different doping ratios of MgCr_2O_4 : (a) TG curves, (b) reaction time, and (c) weight change ratio. DSC curves: (d) MC-5, (e) MC-10, (f) MC-15, and (g) MC-20.

forming new substances with CuO . The FESEM images of the prepared samples are shown in Figure S2. The irregular shape of CuO microparticles and spherical nanosized MgCr_2O_4 particles are obtained. Compared with CuO , the surface of CuO particles was uniformly decorated with more MgCr_2O_4 small grains in the MC-5, MC-10, MC-15, and MC-20 samples, indicating that the MgCr_2O_4 -modified CuO materials were successfully synthesized.

The improvement of the $\text{CuO}/\text{Cu}_2\text{O}$ oxidation performance by MgCr_2O_4 prompter modification is tested by thermogravimetry-differential scanning calorimetry (TG-DSC) (Figure 1). As shown in Figure 1a,c, the weight gain of $\text{CuO}/\text{Cu}_2\text{O}$ is only 4.6% during the oxidation process, and the re-oxidation degree is 46%. However, the oxidation activity of the modified samples had been greatly improved. When the doping amount was only 5 wt % (MC-5), the re-oxidation degree reached 99.9%. The oxidation reaction rate was faster under 5–20 wt % doping ratios (about 4 min on average), while CuO took 13.2 min (Figure 1b). In addition, for every 5 wt % increase in the doping amount of MgCr_2O_4 , the equal proportion of $\text{CuO}/$

Cu_2O in which the redox reaction occurred decreased. Therefore, the weight loss and gain of samples correspondingly decreased by 0.5%. Figure 1d–g shows that the enthalpy changes of the reduction of MC-5, MC-10, MC-15, and MC-20 are -939.42 , -851.09 , -818.23 , and -769.01 kJ/kg and those of the oxidation are 930.40, 842.26, 812.90, and 752.58 kJ/kg, respectively. However, the thermochemical energy release density of CuO is only 466.23 kJ/kg (Figure S3). The results show that the MgCr_2O_4 -modified $\text{CuO}/\text{Cu}_2\text{O}$ has higher thermochemical energy density and excellent reversibility.

3.2. Physicochemical Characterizations during Redox. To clarify the phase change of samples during the redox reaction, XRD tests were carried out at different stages. The strong Cu_2O diffraction peak appeared in the phase composition after oxidation (Figure S4), indicating that more Cu_2O was not oxidized to CuO , resulting in a low re-oxidation degree, which was consistent with the results in Figure 1. Figure 2 presents the XRD patterns of the MC-5, MC-10, MC-15, and MC-20 samples. The phase composition of materials

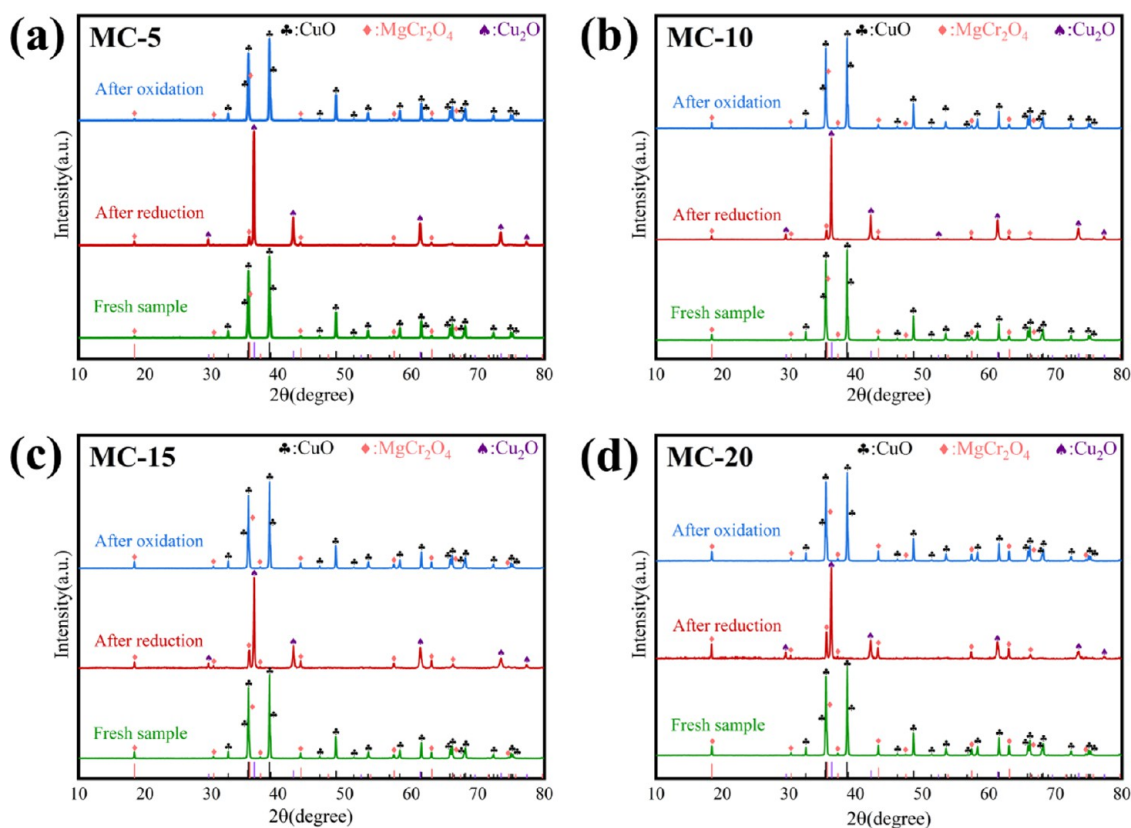


Figure 2. XRD patterns of the samples at different stages: (a) MC-5, (b) MC-10, (c) MC-15, and (d) MC-20.

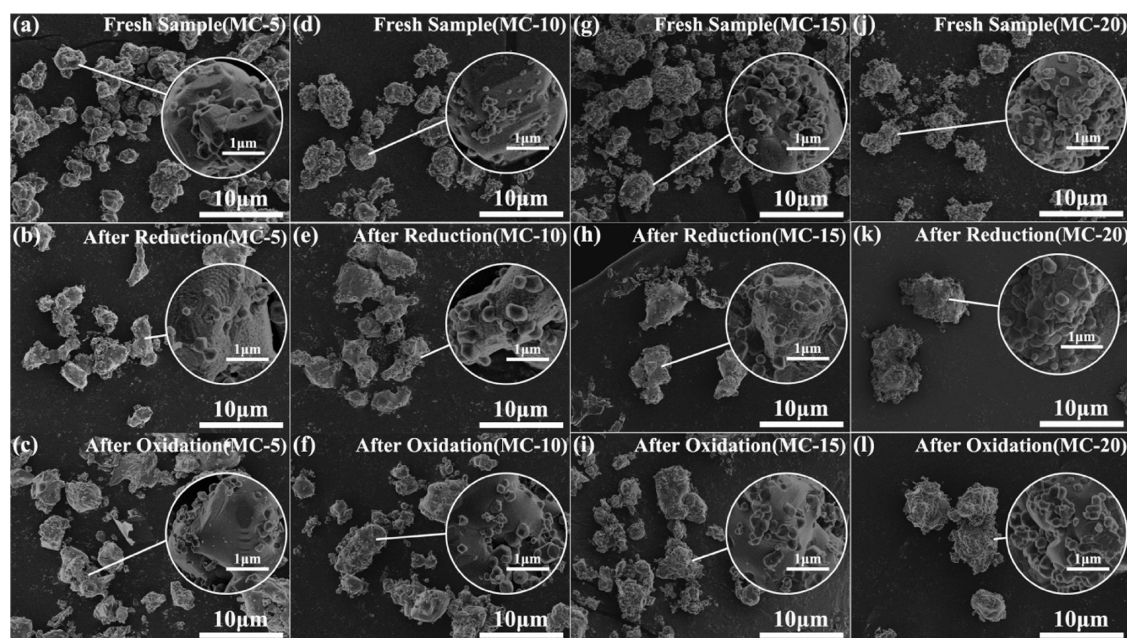


Figure 3. FESEM images of samples at different stages: fresh samples of (a) MC-5, (d) MC-10, (g) MC-15, and (j) MC-20; after reduction of (b) MC-5, (e) MC-10, (h) MC-15, and (k) MC-20; and after oxidation of (c) MC-5, (f) MC-10, (i) MC-15, and (l) MC-20.

with different doping amounts during the reaction was CuO, Cu₂O, and MgCr₂O₄. Cu₂O was completely converted to CuO after oxidation, and the phase composition was consistent with the fresh sample. It demonstrated that MgCr₂O₄ could significantly improve the chemical reaction reversibility. MgCr₂O₄ did not show phase transitions during the whole redox reaction, and the peak diffraction intensity remained

unchanged. Only CuO/Cu₂O underwent the redox reaction. Thus, the chemical reaction process of surface decoration modification by MgCr₂O₄ spinel promoter could be obtained. The promoter has excellent thermal stability in the operating temperature range and does not react with CuO/Cu₂O to form impurities affecting the reaction characteristics. The reaction equation is derived as follows:

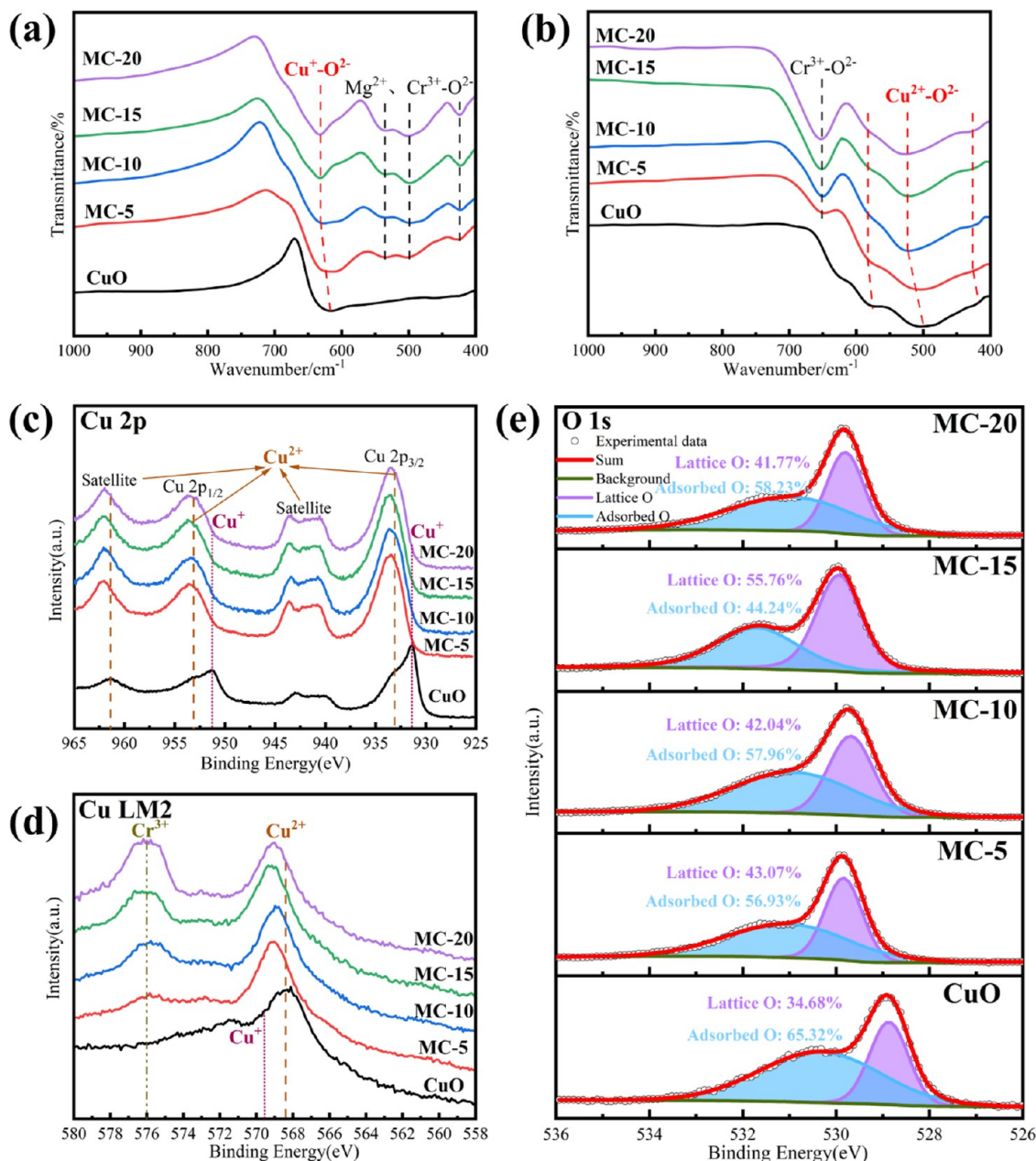
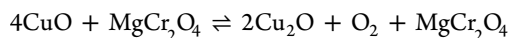


Figure 4. Surface chemistry of different samples. Local enlargement FTIR spectra at the range of 400–1000 cm^{-1} : (a) after reduction and (b) after first cycle oxidation. XPS spectra of (c) Cu 2p, (d) Cu LM2, and (e) O 1s of the samples after the first cycle.



FESEM was used to characterize and analyze the morphology of samples at different stages, which further revealed the mechanism of MgCr_2O_4 surface modification on the improvement of redox reaction performance. The FESEM images of CuO during the redox reaction are presented in Figure S5. Coalescence between CuO particles led to densification, forming large particles with irregular shapes. It is speculated that due to the densification of the larger particles, oxygen absorbs and reacts on the surface of the particles but is difficult to diffuse into the interior, resulting in the inability to completely oxidize Cu_2O to CuO. The crystal morphology changes of the MC-5, MC-10, MC-15, and MC-20 samples at different stages are shown in Figure 3. In the whole redox reaction process with various doping ratios,

MgCr_2O_4 was uniformly decorated on the CuO/ Cu_2O surface, indicating that MgCr_2O_4 and CuO/ Cu_2O had a strong interaction. Even when CuO/ Cu_2O underwent a phase change during the reaction, MgCr_2O_4 was not easy to detach and coalesce while maintaining the phase structure stability and was evenly distributed on the CuO/ Cu_2O surface. Moreover, the decoration of nanosized MgCr_2O_4 on the surface of metal oxides can ensure that there is a larger reaction area between the materials and air and effectively prevent the coalescence and sintering caused by the mutual contact between CuO/ Cu_2O grains. The particle size of the MgCr_2O_4 -modified materials after reaction were all $\sim 4\text{--}6\ \mu\text{m}$, which was about 1/4 of that of CuO ($\sim 19\text{--}20\ \mu\text{m}$). Therefore, doping MgCr_2O_4 can effectively improve the reaction performance of CuO/ Cu_2O .

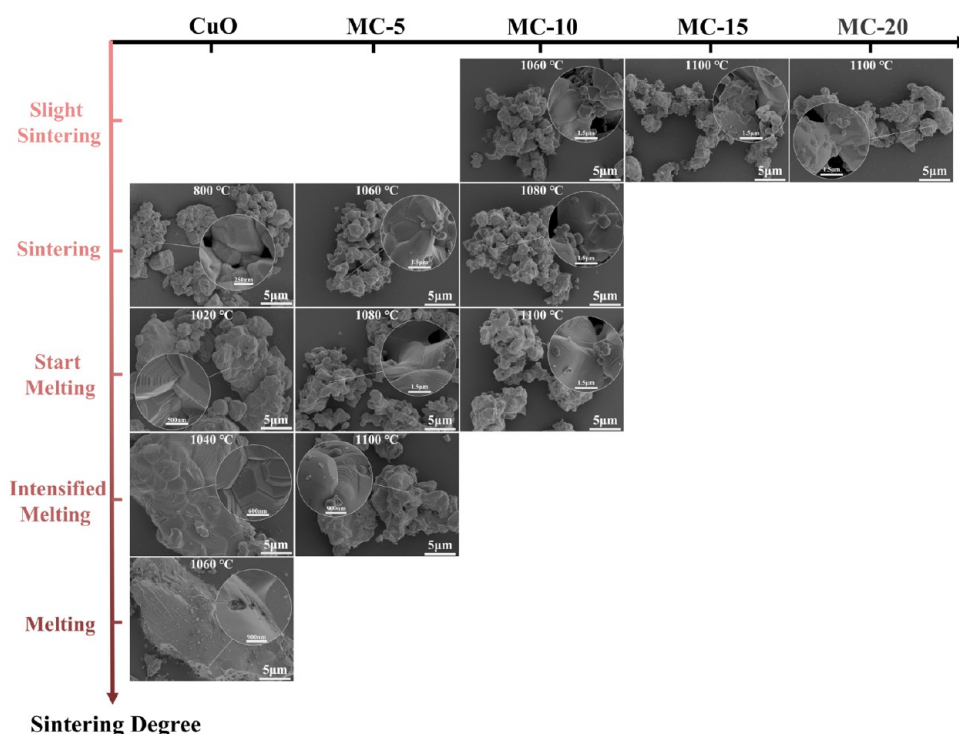


Figure 5. Sintering degree of samples in the operating temperature range.

The surface chemistry properties of different samples are shown in Figure 4. The local enlargement FTIR spectra in the range of 400–1000 cm^{-1} have been presented in Figure 4a,b. The detailed FTIR spectra at 400–4000 cm^{-1} are shown in Figure S6. The peaks at 423, 499, 534, and 652 cm^{-1} on the MC samples could be attributed to the lattice vibrations of $\text{Mg}^{2+}-\text{O}^{2-}$ and $\text{Cr}^{3+}-\text{O}^{2-}$ at the tetrahedral and octahedral sites of the spinel structure.^{34–36} With the increase in the MgCr_2O_4 doping content, the Mg^{2+} and $\text{Cr}^{3+}-\text{O}^{2-}$ peak intensities increased gradually. Bands were observed at 616–631 cm^{-1} , arising from the vibrations of $\text{Cu}^+-\text{O}^{2-}$ at the samples after reduction.³⁷ For the oxidized samples, there were strong absorption peaks at 417–427, 505–522, and 576–583 cm^{-1} , corresponding to characteristic stretching vibrations of the $\text{Cu}^{2+}-\text{O}^{2-}$ bond in monoclinic CuO .^{38,39} It was worth noting that the position of the $\text{Cu}-\text{O}$ peak in MC samples at different stages shifted to a higher wavenumber, suggesting a strong interaction between $\text{Cu}_2\text{O}/\text{CuO}$ and MgCr_2O_4 . Therefore, the promoter can be firmly combined with $\text{Cu}_2\text{O}/\text{CuO}$, which is not easy to detach and coalesce during the cycle, inhibiting the migration and sintering of $\text{Cu}_2\text{O}/\text{CuO}$.

The XPS results of different samples after the first cycle were used to further evaluate their re-oxidation. The XPS spectra of Cu 2p are detailed in Figure 4c, where the peaks split into Cu 2p_{1/2} and Cu 2p_{3/2} along with the satellites, respectively. The peaks at 931.4 and 951.3 eV were associated with Cu^+ species.⁴⁰ The binding energies of 933.2 and 953.2 eV and the shake-up satellites correspond to Cu^{2+} .⁴¹ MC-5, MC-10, MC-15, and MC-20 had stronger satellite and Cu^{2+} peaks, and no obvious Cu^+ peak appeared, further proving that the oxidation reaction of the MgCr_2O_4 -modified samples was more complete. The Cu LM2 spectra are shown in Figure 4d, with peaks at 568.4 and 569.5 eV attributed to CuO and Cu_2O , respectively.⁴² Consistent with the results of Cu 2p analysis, the undoped CuO sample after the first cycle had an obvious

Cu^+ peak, which further proved its poor re-oxidation performance together with Figure S4. In addition, there was a Cr^{3+} characteristic peak at 576 eV in the modified samples.⁴³ Compared with CuO , the peaks of MC-5, MC-10, MC-15, and MC-20 shifted to the higher binding energy. The shift indicates some alterations in the electronic properties of copper species, suggesting that there is a charge transfer between CuO and the promoter. The electron binding energy shift of Cu 2p and Cu LM2 reveals a strong interaction between CuO and MgCr_2O_4 , which is consistent with FTIR analysis. Two typical peaks at 528.9–529.9 and 530.4–531.6 eV in the O 1s spectra of Figure 4e can be attributed to lattice oxygen and adsorbed oxygen, which includes oxygen defects or a mixture of hydroxyl groups on the surface of CuO .⁴⁴ The lattice oxygen content of CuO after oxidation was 34.68%, while those of MC-5, MC-10, MC-15, and MC-20 increased to 43.07, 42.04, 55.76, and 41.77%, respectively. It should be noted that the adsorption and release of lattice oxygen are the rate-determining steps in the redox reaction.⁴⁵ Therefore, the increase of active lattice oxygen content is conducive to promoting the redox cycle.

3.3. Sintering Amelioration. The sintering of the samples in the operating temperature range is shown in Figures S7 and 5. The CuO powder appeared to be significantly sintered at 800 °C to form coacervates ($\sim 10 \mu\text{m}$), melting began at 1020 °C and particle growth ($\sim 14 \mu\text{m}$), further intensified sintering and melting at 1040 °C produced densified lumps ($\sim 22 \mu\text{m}$), and completely melting at 1060 °C ($\sim 26 \mu\text{m}$). CuO did not melt before reduction, resulting in only severe sintering. It started to melt at the reduction temperature of about 1020 °C and was completely reduced to Cu_2O . However, Cu_2O has poor thermal stability and a lower melting point. Accordingly, it is speculated that the melting might be caused by Cu_2O and the sintering of CuO in the early stage promoted melting. The chemical reaction contact area between the material and the air decreased sharply, resulting in poor performance. Surprisingly,

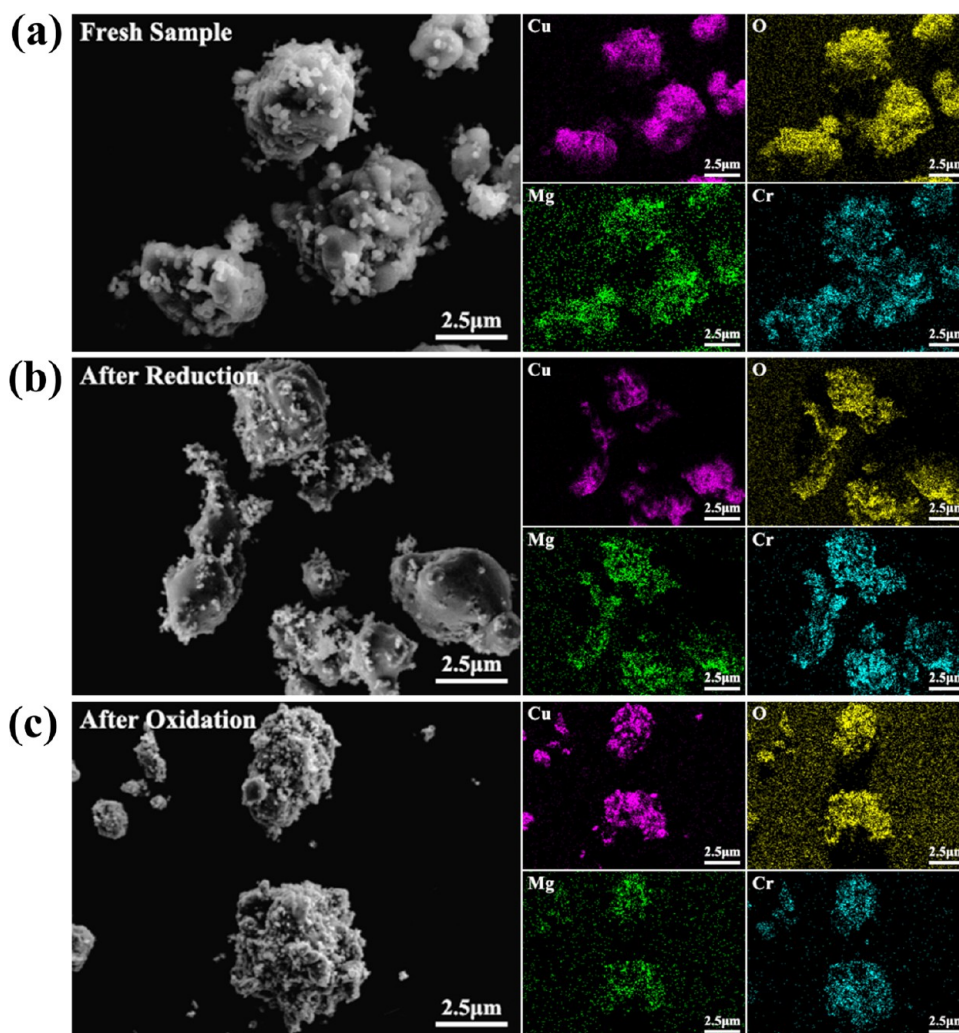


Figure 6. SEM images and the corresponding EDS mapping of MC-15 at different stages: (a) fresh sample; (b) after reduction; and (c) after oxidation.

samples doped with 5–20 wt % MgCr_2O_4 were significantly less sintered than undoped CuO . Consistent with the above results, the re-oxidation performance of all doped MgCr_2O_4 samples was improved due to the mitigation of sintering. However, the MC-5 sample showed more severe melting at $1100\text{ }^\circ\text{C}$ (particle size $\sim 11\text{ }\mu\text{m}$), so the redox results (Figure 1a,b) showed a relatively slow re-oxidation rate. MC-10 also demonstrated a slightly melting at $1100\text{ }^\circ\text{C}$ ($\sim 8\text{ }\mu\text{m}$), which had little effect on the first re-oxidation performance. However, MC-5 and MC-10 certainly could not be recycled because cycling at high temperatures further exacerbated melting, resulting in attenuation of cycle life. Only slight sintering was observed for MC-15 ($\sim 4\text{ }\mu\text{m}$) and MC-20 ($\sim 5\text{ }\mu\text{m}$) during operating temperature. As shown in Figure 1f,g, $\text{CuO}/\text{Cu}_2\text{O}$ decreased with the increase of MgCr_2O_4 doping, thus reducing the energy storage density. MC-15 significantly increased the sintering temperature of $\text{CuO}/\text{Cu}_2\text{O}$ while considering higher energy density. Therefore, 15 wt % MgCr_2O_4 is the optimal doping amount.

EDS mapping was used to observe the distribution of prompter on the $\text{CuO}/\text{Cu}_2\text{O}$ surface to explain the mechanism of slowing sintering. The EDS mapping of MC-15 at different stages is shown in Figures 6 and S8. The elemental mapping further revealed that the MgCr_2O_4 prompter was uniformly

distributed on the surface of $\text{CuO}/\text{Cu}_2\text{O}$ particles as a separate phase. The more uniform the prompter was decorated, the physical barrier effect could be maximized to prevent particle coalescence, thereby promoting the sintering resistance of the material. Meanwhile, no obvious CuO , Cu_2O , or MgCr_2O_4 coalescence was observed in the whole reaction process, indicating that $\text{CuO}/\text{Cu}_2\text{O}$ and MgCr_2O_4 were more attractive to each other. Therefore, the phenomenon of material densification can be avoided, which is caused by the migration of the substance after the bonding between $\text{CuO}-\text{CuO}$ or $\text{Cu}_2\text{O}-\text{Cu}_2\text{O}$ particles to produce strength in the powder. To further demonstrate the sintering resistance of MC-15, the sample with physical mixing of 15 wt % MgCr_2O_4 and 85 wt % CuO was labeled as PX-MC-15 for comparison with MC-15. As shown in Figure S9, the particle size of PX-MC-15 was about $23\text{ }\mu\text{m}$ after calcination at $1100\text{ }^\circ\text{C}$. Compared with undoped CuO ($\sim 26\text{ }\mu\text{m}$ at $1060\text{ }^\circ\text{C}$), it indicates that the steric hindrance effect of MgCr_2O_4 on CuO can alleviate sintering to a certain extent. However, its particle size was about 5.8 times that of MC-15 ($\sim 4\text{ }\mu\text{m}$ at $1100\text{ }^\circ\text{C}$). The uneven distribution of MgCr_2O_4 on the CuO surface was obviously observed in the fresh sample and the PX-MC-15 sample at $1100\text{ }^\circ\text{C}$. There were many MgCr_2O_4 and CuO coacervates, which did not conform to the material structure

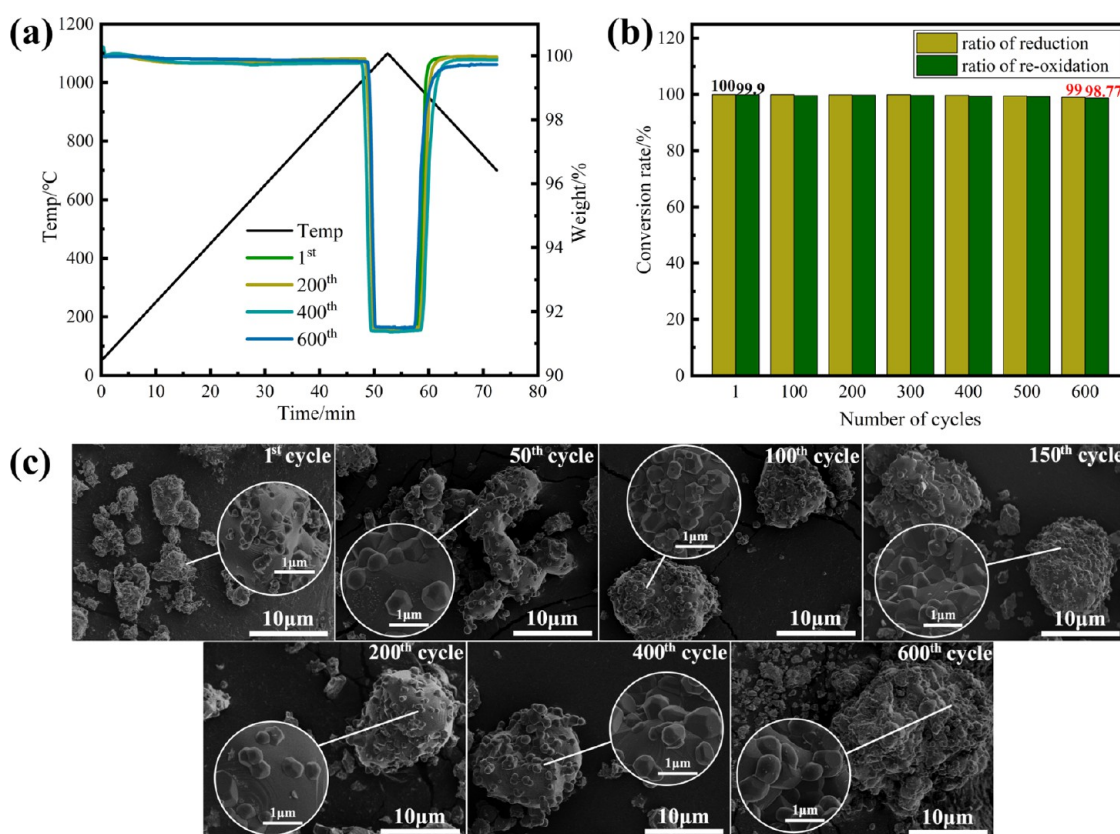


Figure 7. Long-life cycling performance of MC-15. (a) TG curves, (b) conversion rate, and (c) FESEM images with different cycles.

we proposed. In brief, the sintering amelioration of the material was closely related to the surface modification amount, dispersion uniformity of the promoter, and its interaction with sinter-prone substances.

3.4. Cycling Life. The long-life cyclic performance of MC-15 is shown in Figure 7. A cycle refers to the achievement of a complete redox process of the material. After 600 cycles, the reduction degree of MC-15 reached 99% of the initial reaction value, and the re-oxidation degree remained at 98.77% (Figure 7a,b). The re-oxidation degree of CuO decreased to 28% only after 40 cycles (Figure S10), which was 1.6 times less than that of the first cycle and had a fast decay rate.

SEM was used to observe the changes in grain morphology after multiple cycles, and the effect of sintering on the cycle performance was explored. There was serious agglomeration and sintering between CuO particles after only 10 cycles (Figure S11). With the progress of the cycle, the grain fusion and grain boundary blurred, and the sintered body was obviously densified after 40 cycles. The FESEM images of MC-15 after different cycles are shown in Figure 7c. The relatively large particle size of MC-15 after 600 cycles was about 19 μm, which was comparable to that of CuO after 20 cycles (~20 μm). In addition, MgCr₂O₄ had been uniformly decorated on the CuO surface to ensure the physical barrier effect even after multiple redox cycles, further demonstrating the strong interaction between MgCr₂O₄ and CuO/Cu₂O. Overall, MgCr₂O₄ effectively alleviates the sintering of CuO/Cu₂O so that the material still has excellent cycle stability in a high-temperature working environment.

The change in the specific surface area of the material after multiple cycles was tested to jointly verify the improvement effect of MgCr₂O₄-modified samples on cycle performance.

The specific surface area change after different cycles is listed in Table 1. The specific surface area of CuO was 1.1 m²/g after

Table 1. Specific Surface Area Change after Different Cycles

metal oxides	cycle number	BET (m ² /g)
CuO	1	1.1
	20	0.8
	40	0.3
MC-15	1	1.9
	200	1.1
	400	1.0
	600	0.7

the first cycle, but it decreased to 0.3 m²/g after only 40 cycles. With the increase in the number of cycles at high temperatures, severe sintering of CuO led to densification and growth of particles, causing a sharp decrease in its specific surface area. The BET surface area of MC-15 after one cycle was 1.9 m²/g, which might be due to the small particle size of the MgCr₂O₄ promoter (nanosized) loaded on the surface of CuO, resulting in its specific surface area being slightly larger than that of CuO. Surprisingly, the specific surface area of MC-15 after 600 cycles remained 0.7 m²/g, which was 2.3 times larger than that of CuO after 40 cycles. It was further confirmed that MC-15 can effectively alleviate sintering and limit the aggregation and growth of particles, thus ensuring the chemical reaction contact area of CuO/Cu₂O. Therefore, MC-15 has excellent reactivity and cycle life.

3.5. Modification Mechanism. All of the aforementioned results confirmed the interaction between CuO/Cu₂O and MgCr₂O₄, which significantly increasing the sintering temper-

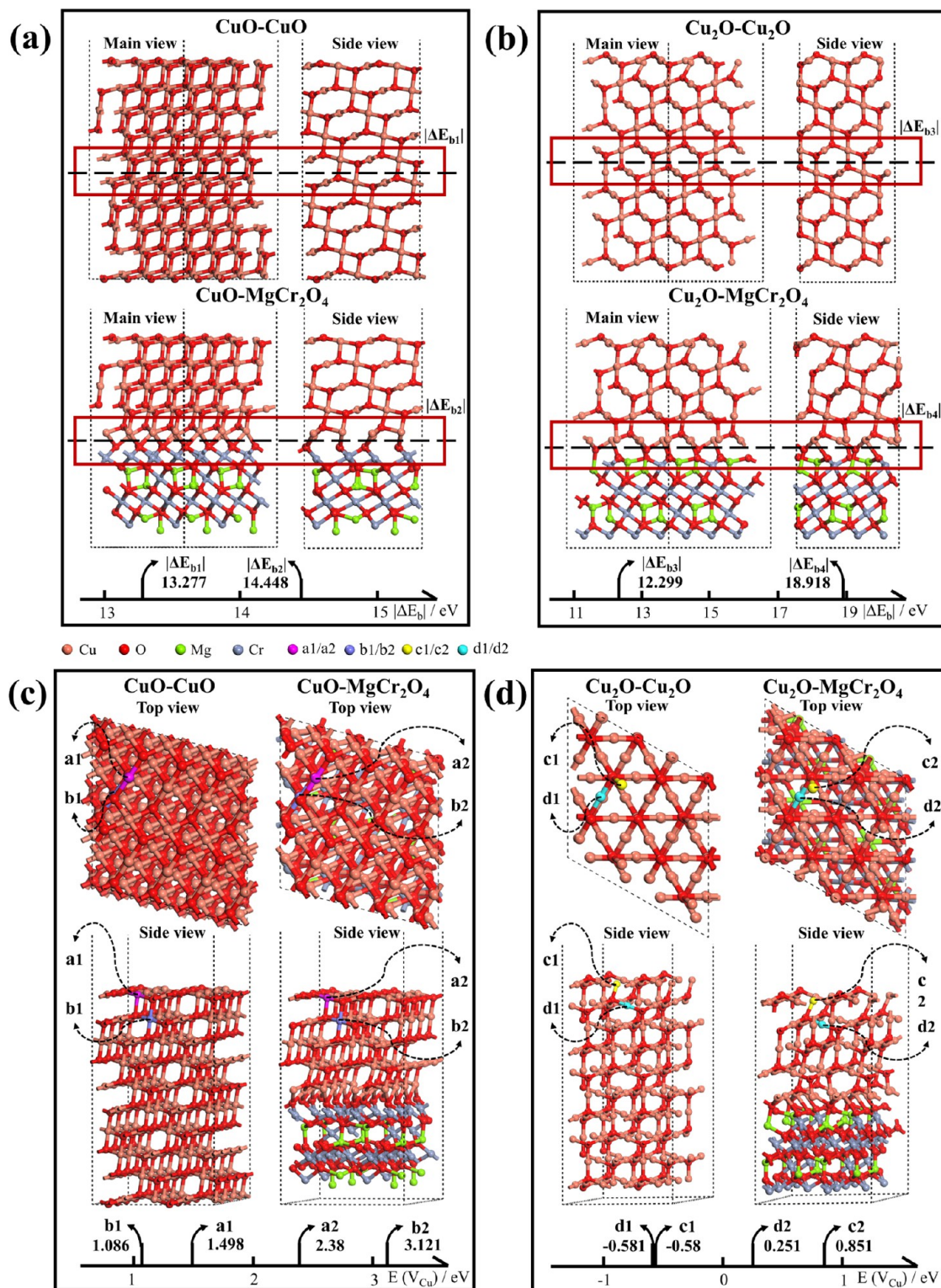


Figure 8. DFT calculations. The absolute value of interface binding energy $|\Delta E_b|$ of (a) CuO–CuO and CuO–MgCr₂O₄ and (b) Cu₂O–Cu₂O and Cu₂O–MgCr₂O₄. Formation energies of copper vacancy $E(V_{Cu})$ at different sites of (c) CuO–CuO and CuO–MgCr₂O₄, (d) Cu₂O–Cu₂O, and Cu₂O–MgCr₂O₄.

ature and greatly improving the reaction performance. Therefore, DFT calculations are carried out to further reveal the mechanism of antisintering modification (Figure 8). Different CuO/Cu₂O–MgCr₂O₄ interface structure models are constructed (Figure S12). As shown in Figure 8a,b, the absolute values of interface binding energy $|\Delta E_b|$ has the order

of CuO–CuO < CuO–MgCr₂O₄ and Cu₂O–Cu₂O < Cu₂O–MgCr₂O₄. It indicates that compared with CuO–CuO and Cu₂O–Cu₂O self-binding, CuO/Cu₂O is easier to combine with MgCr₂O₄ and the system is more stable, which can alleviate the sintering caused by surface contact and bonding. In addition, the bond lengths of Cu–O and Cr–O bonds at

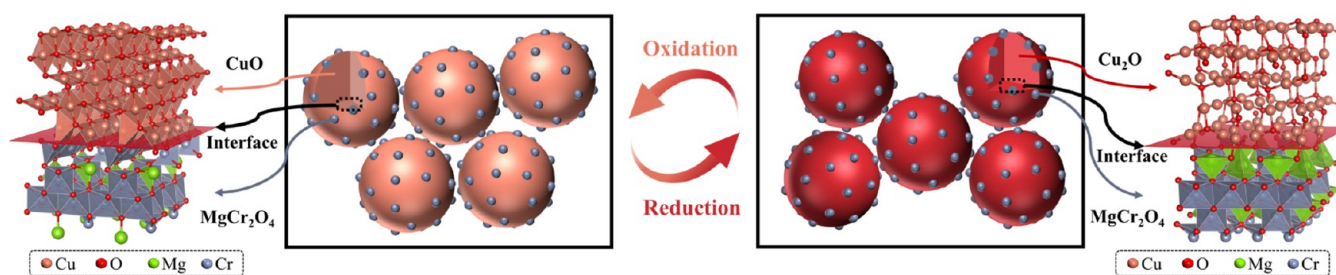


Figure 9. Schematic of the CuO/Cu₂O reaction modification mechanism of the surface-decorated MgCr₂O₄ spinel prompter.

the interface after optimization of different models are listed in Table S4. After the combination of CuO/Cu₂O and MgCr₂O₄, the bond length was shortened and the bond energy was enhanced, which verified the strong interaction between metal oxides and prompter. It can inhibit the migration and coalescence tendency of CuO/Cu₂O at high temperatures. Also, the prompter is not easy to detach in the cycle, ensuring its spatial confinement effect. According to the mass transfer through diffusion mechanism in solid state sintering theory, the vacancy concentration of each part of the particle has a certain difference, and the concentration gradient promotes the diffusion and migration of thermal defects such as vacancy on the surface or inside of the particles, thus accelerating sintering. Consequently, the formation energies of copper vacancy at different positions were calculated and compared. The results are illustrated in Figure 8c,d. The formation energies of copper vacancy in different atomic layers of the CuO/Cu₂O–MgCr₂O₄ structure are greater than those of CuO/Cu₂O. The formation of copper vacancies in CuO/Cu₂O after the surface modification of MgCr₂O₄ became more difficult, thus retarding sintering. These calculations theoretically elucidate that the introduction of the MgCr₂O₄ prompter can effectively resist sintering by enhancing the interaction between metal oxides and prompter and increasing the copper vacancy formation energy of metal oxides.

As shown in Figure 9, the CuO/Cu₂O reaction modification mechanism of surface-decorated MgCr₂O₄ spinel prompter is obtained by combining material characterization and DFT calculations. MgCr₂O₄ is uniformly loaded on the surface of CuO/Cu₂O and does not react with CuO/Cu₂O to maintain phase stability throughout the reversible reaction. The driving force of CuO/Cu₂O grain growth is countered by the pinning force of inert prompter MgCr₂O₄ on the grain boundary, which can effectively inhibit grain growth. Moreover, MgCr₂O₄ effectively plays the physical barrier role of the prompter to prevent the active component particles from sintering without destroying redox activity. In addition, CuO/Cu₂O and MgCr₂O₄ have a large interfacial interaction intensity due to the strong interaction between metal oxides and prompter. It inhibits the migration and sintering of materials and enables a firm bond between prompter and metal oxides, thus ensuring the high reactivity and long cycle life of metal oxides that are easy to sinter at high temperatures.

4. CONCLUSIONS

In summary, we have successfully synthesized MgCr₂O₄-modified CuO/Cu₂O material with a significantly improved re-oxidation performance of Cu₂O at high temperatures. The oxidation rate of the 15 wt % MgCr₂O₄-modified material was increased by 3.7 times, with the re-oxidation degree reaching 99.9%. The chemical energy density of storage and release

reached −818.23 and 812.90 kJ/kg. The experimental test elucidated that the prompter was uniformly distributed on the CuO/Cu₂O surface, and there is a strong interaction between them, which effectively solves the problem of severe sintering in the working temperature range. Moreover, MgCr₂O₄ increased the lattice oxygen content of the material and promoted oxidation reactivity. After 600 cycles, the oxidation activity remained 98.77%. DFT calculation results further verified the strong binding relationship, and copper vacancies in CuO/Cu₂O were more difficult to form after MgCr₂O₄ modification. The mechanism of antisintering and reaction modification was revealed by combining material characterizations and theoretical calculations. Through deep research of the relationship between CuO/Cu₂O and MgCr₂O₄ spinel prompter, this work provides a facile and efficient design strategy for the development and operation of high-performance thermochemical energy storage materials, which can be extended to synthesize other sintering-resistant metal oxides.

■ ASSOCIATED CONTENT

Supporting Information

The Supporting Information is available free of charge at <https://pubs.acs.org/doi/10.1021/acsami.2c09519>.

Details of XRD patterns, TGA-DSC measurements, SEM images, FTIR spectra, EDS spectra, and DFT calculations (PDF)

■ AUTHOR INFORMATION

Corresponding Author

Gang Xiao – State Key Laboratory of Clean Energy Utilization, College of Energy Engineering, Zhejiang University, Hangzhou, Zhejiang 310027, China;
 orcid.org/0000-0001-6761-8380;
 Email: xiaogangtianmen@zju.edu.cn

Authors

Jiali Deng – State Key Laboratory of Clean Energy Utilization, College of Energy Engineering, Zhejiang University, Hangzhou, Zhejiang 310027, China
 Changdong Gu – State Key Laboratory of Silicon Materials, College of Materials Science and Engineering, Zhejiang University, Hangzhou, Zhejiang 310027, China;
 orcid.org/0000-0001-8286-263X
 Haoran Xu – State Key Laboratory of Clean Energy Utilization, College of Energy Engineering, Zhejiang University, Hangzhou, Zhejiang 310027, China

Complete contact information is available at: <https://pubs.acs.org/doi/10.1021/acsami.2c09519>

Author Contributions

J.D. was responsible for conceptualization, methodology, software, investigation, and writing the original draft. C.G. validated the study and wrote, reviewed, and edited the manuscript. H.X. visualized the experiment and wrote, reviewed, and edited the manuscript. G.X. was responsible for the resources, supervision, project administration, and funding acquisition.

Notes

The authors declare no competing financial interest.

ACKNOWLEDGMENTS

This work was supported by the Zhejiang Science Foundation for Distinguished Young Scholars (LR20E060001) and the National Natural Science Foundation of China (52176207).

REFERENCES

- (1) Gençer, E.; Agrawal, R. Synthesis of Efficient Solar Thermal Power Cycles for Baseload Power Supply. *Energy Convers. Manage.* **2017**, *133*, 486–497.
- (2) Weinstein, L. A.; Loomis, J.; Bhatia, B.; Bierman, D. M.; Wang, E. N.; Chen, G. Concentrating Solar Power. *Chem. Rev.* **2015**, *115*, 12797–12838.
- (3) André, L.; Abanades, S.; Flamant, G. Screening of Thermochemical Systems Based on Solid–Gas Reversible Reactions for High Temperature Solar Thermal Energy Storage. *Renewable Sustainable Energy Rev.* **2016**, *64*, 703–715.
- (4) Solé, A.; Martorell, I.; Cabeza, L. F. State of the Art on Gas-solid Thermochemical Energy Storage Systems and Reactors for Building Applications. *Renewable Sustainable Energy Rev.* **2015**, *47*, 386–398.
- (5) Agrafiotis, C.; Roeb, M.; Sattler, C. Hybrid Sensible/thermochemical Solar Energy Storage Concepts Based on Porous Ceramic Structures and Redox Pair Oxides Chemistry. *Energy Procedia* **2015**, *69*, 706–715.
- (6) Lanchi, M.; Turchetti, L.; Sau, S.; Liberatore, R.; Cerbelli, S.; Murmura, M. A.; Annesini, M. C. A Discussion of Possible Approaches to the Integration of Thermochemical Storage Systems in Concentrating Solar Power Plants. *Energies* **2020**, *13*, No. 4940.
- (7) Carrillo, A. J.; González-Aguilar, J.; Romero, M.; Coronado, J. M. Solar Energy on Demand: A Review on High Temperature Thermochemical Heat Storage Systems and Materials. *Chem. Rev.* **2019**, *119*, 4777–4816.
- (8) Wu, S.; Zhou, C.; Doroodchi, E.; Nellore, R.; Moghtaderi, B. A Review on High-temperature Thermochemical Energy Storage Based on Metal Oxides Redox Cycle. *Energy Convers. Manage.* **2018**, *168*, 421–453.
- (9) Prasad, J. S.; Muthukumar, P.; Desai, F.; Basu, D. N.; Rahman, M. M. A Critical Review of High-temperature Reversible Thermochemical Energy Storage Systems. *Appl. Energy* **2019**, *254*, No. 113733.
- (10) André, L.; Abanades, S.; Cassayre, L. Experimental Investigation of Co–Cu, Mn–Co, and Mn–Cu Redox Materials Applied to Solar Thermochemical Energy Storage. *ACS Appl. Energy Mater.* **2018**, *1*, 3385–3395.
- (11) Liu, J.; Baeyens, J.; Deng, Y.; Wang, X.; Zhang, H. High Temperature Mn_2O_3/Mn_3O_4 and Co_3O_4/CoO Systems for Thermochemical Energy Storage. *J. Environ. Manage.* **2020**, *267*, No. 110582.
- (12) Agrafiotis, C.; Tescari, S.; Roeb, M.; Schmücker, M.; Sattler, C. Exploitation of Thermochemical Cycles Based on Solid Oxide Redox Systems for Thermochemical Storage of Solar Heat. Part 3: Cobalt Oxide Monolithic Porous Structures as Integrated Thermochemical Reactors/heat Exchangers. *Sol. Energy* **2015**, *114*, 459–475.
- (13) Muroyama, A. P.; Schrader, A. J.; Loutzenhiser, P. G. Solar Electricity Via an Air Brayton Cycle with an Integrated Two-step Thermochemical Cycle for Heat Storage Based on Co_3O_4/CoO Redox Reactions II: Kinetic Analyses. *Sol. Energy* **2015**, *122*, 409–418.
- (14) Müller, D.; Knoll, C.; Artner, W.; Harasek, M.; Gierl-Mayer, C.; Welch, J. M.; Werner, A.; Weinberger, P. Combining In situ X-ray Diffraction with Thermogravimetry and Differential Scanning Calorimetry—An Investigation of Co_3O_4 , MnO_2 and PbO_2 for Thermochemical Energy Storage. *Sol. Energy* **2017**, *153*, 11–24.
- (15) Yilmaz, D.; Darwish, E.; Leion, H. Investigation of the Combined Mn–Si Oxide System for Thermochemical Energy Storage Applications. *J. Energy Storage* **2020**, *28*, No. 101180.
- (16) Bielsa, D.; Zaki, A.; Arias, P. L.; Faik, A. Improving the Redox Performance of Mn_2O_3/Mn_3O_4 Pair by Si Doping to be Used as Thermochemical Energy Storage for Concentrated Solar Power Plants. *Sol. Energy* **2020**, *204*, 144–154.
- (17) Randhir, K.; King, K.; Rhodes, N.; Li, L.; Hahn, D.; Mei, R.; Yeung, N. A.; Klausner, J. Magnesium–manganese Oxides for High Temperature Thermochemical Energy Storage. *J. Energy Storage* **2019**, *21*, 599–610.
- (18) Xiang, D.; Gu, C. D.; Xu, H. R.; Xiao, G. Self-Assembled Structure Evolution of Mn–Fe Oxides for High Temperature Thermochemical Energy Storage. *Small* **2021**, *17*, No. 2101524.
- (19) Carrillo, A. J.; Pizarro, P.; Coronado, J. M. Assessing Cr Incorporation in Mn_2O_3/Mn_3O_4 Redox Materials for Thermochemical Heat Storage Applications. *J. Energy Storage* **2021**, *33*, No. 102028.
- (20) Neises, M.; Tescari, S.; de Oliveira, L.; Roeb, M.; Sattler, C.; Wong, B. Solar-heated Rotary Kiln for Thermochemical Energy Storage. *Sol. Energy* **2012**, *86*, 3040–3048.
- (21) Jahromy, S. S.; Birkelbach, F.; Jordan, C.; Huber, C.; Harasek, M.; Werner, A.; Winter, F. Impact of Partial Pressure, Conversion, and Temperature on the Oxidation Reaction Kinetics of Cu_2O to CuO in Thermochemical Energy Storage. *Energies* **2019**, *12*, No. 508.
- (22) Alonso, E.; Pérez-Rábago, C.; Licurgo, J.; Fuentealba, E.; Estrada, C. A. First Experimental Studies of Solar Redox Reactions of Copper Oxides for Thermochemical Energy Storage. *Sol. Energy* **2015**, *115*, 297–305.
- (23) Deutsch, M.; Horvath, F.; Knoll, C.; Lager, D.; Gierl-Mayer, C.; Weinberger, P.; Winter, F. High-temperature Energy Storage: Kinetic Investigations of the CuO/Cu_2O Reaction Cycle. *Energy Fuels* **2017**, *31*, 2324–2334.
- (24) Block, T.; Schmücker, M. Metal Oxides for Thermochemical Energy Storage: A Comparison of Several Metal Oxide Systems. *Sol. Energy* **2016**, *126*, 195–207.
- (25) Imtiaz, Q.; Broda, M.; Müller, C. R. Structure-property Relationship of Co-precipitated Cu-rich, Al_2O_3 - or $MgAl_2O_4$ -Stabilized Oxygen Carriers for Chemical Looping with Oxygen Uncoupling (CLOU). *Appl. Energy* **2014**, *119*, 557–565.
- (26) Xiang, D.; Gu, C. D.; Xu, H. R.; Deng, J. L.; Zhu, P. W.; Xiao, G. Al-Modified CuO/Cu_2O for High-Temperature Thermochemical Energy Storage: from Reaction Performance to Modification Mechanism. *ACS Appl. Mater. Interfaces* **2021**, *13*, 57274–57284.
- (27) Kresse, G.; Furthmüller, J. Efficient Iterative Schemes for Ab Initio Total-energy Calculations Using a Plane-wave Basis Set. *Phys. Rev. B* **1996**, *54*, 11169–11186.
- (28) Perdew, J. P.; Burke, K.; Ernzerhof, M. Generalized Gradient Approximation Made Simple. *Phys. Rev. Lett.* **1996**, *77*, 3865–3868.
- (29) Kresse, G.; Joubert, D. From Ultrasoft Pseudopotentials to the Projector Augmented-wave Method. *Phys. Rev. B* **1999**, *59*, No. 1758.
- (30) Dudarev, S. L.; Botton, G. A.; Savrasov, S. Y.; Humphreys, C. J.; Sutton, A. P. Electron-energy-loss Spectra and the Structural Stability of Nickel Oxide: An LSDA+ U Study. *Phys. Rev. B* **1998**, *57*, No. 1505.
- (31) Nolan, M.; Elliott, S. D. The p-Type Conduction Mechanism in Cu_2O : A First Principles Study. *Phys. Chem. Chem. Phys.* **2006**, *8*, 5350–5358.
- (32) Gao, Y.; Zhang, L.; Van Hoof, A. J.; Friedrich, H.; Hensen, E. J. A Robust $Au/ZnCr_2O_4$ Catalyst with Highly Dispersed Gold Nanoparticles for Gas-Phase Selective Oxidation of Cyclohexanol to Cyclohexanone. *ACS Catal.* **2019**, *9*, 11104–11115.
- (33) Zhao, P.; Ehara, M.; Satsuma, A.; Sakaki, S. Theoretical Insight into Oxidation Catalysis of Chromite Spinel MCr_2O_4 ($M = Mg, Co$,

Cu, and Zn): Volcano Plot for Oxygen-vacancy Formation and Catalytic Activity. *J. Catal.* **2021**, *393*, 30–41.

(34) Mao, L.; Cui, H.; Miao, C.; An, H.; Zhai, J.; Li, Q. Preparation of MgCr_2O_4 from Waste Tannery Solution and Effect of Sulfate, Chloride, and Calcium on Leachability of Chromium. *J. Mater. Cycles Waste Manage.* **2016**, *18*, 573–581.

(35) Lotfian, N.; Nourbakhsh, A.; Mirsattari, S. N.; Mackenzie, K. J. Functionalization of $\text{NiO-MgCr}_2\text{O}_4$ Additives by Silanol Groups: A New Approach to the Development of Magnesia-chrome Refractories. *Ceram. Int.* **2021**, *47*, 31724–31731.

(36) Mykhailovych, V.; Kanak, A.; Cojocar, S.; Chitoiu-Arsene, E. D.; Palamaru, M. N.; Iordan, A. R.; Korovyanko, O.; Diaconu, A.; Ciobanu, V. G.; Caruntu, G.; Lushchak, O.; Fochuk, P.; Khalavka, Y.; Rotaru, A. Structural, Optical, and Catalytic Properties of MgCr_2O_4 Spinel-Type Nanostructures Synthesized by Sol–Gel Auto-Combustion Method. *Catalysts* **2021**, *11*, No. 1476.

(37) Khan, M. A.; Ullah, M.; Iqbal, T.; Mahmood, H.; Khan, A. A.; Shafique, M.; Majid, A.; Ahmed, A.; Khan, N. A. Surfactant Assisted Synthesis of Cuprous Oxide (Cu_2O) Nanoparticles Via Solvothermal Process. *Nanosci. Nanotechnol. Res.* **2015**, *3*, 16–22.

(38) Shinde, S. K.; Dubal, D. P.; Ghodake, G. S.; Gomez-Romero, P.; Kim, S.; Fulari, V. J. Influence of Mn Incorporation on the Supercapacitive Properties of Hybrid CuO/Cu(OH)_2 Electrodes. *RSC Adv.* **2015**, *5*, 30478–30484.

(39) Iqbal, T.; ur Rehman, A.; Khan, M. A.; Shafique, M.; Ahmad, P.; Mahmood, H.; Naeem, M.; Iqbal, J. Copper oxide nanosheets prepared by facile microplasma electrochemical technique with photocatalytic and bactericidal activities. *J. Mater. Sci. Mater. Electron.* **2020**, *31*, 16649–16660.

(40) Tang, X.; He, B.; Li, J.; Qin, G. One-step Preparation of Cu/BC Catalyzed the Upgrading of Heavy Oil Assisted by Microwave. *J. Pet. Sci. Eng.* **2022**, *208*, No. 109683.

(41) Wang, K.; Dong, X.; Zhao, C.; Qian, X.; Xu, Y. Facile Synthesis of $\text{Cu}_2\text{O/CuO/RGO}$ Nanocomposite and Its Superior Cyclability in Supercapacitor. *Electrochim. Acta* **2015**, *152*, 433–442.

(42) Yang, X.; Liu, W.; Pan, G.; Sun, Y. Modulation of Oxygen in NiO : Cu Films toward A Physical Insight of NiO : Cu/c-Si Heterojunction Solar Cells. *J. Mater. Sci.* **2018**, *53*, 11684–11693.

(43) Maitra, S.; Mitra, R.; Nath, T. K. Sol-gel Derived MgCr_2O_4 Nanoparticles for Aqueous Supercapacitor and Alkaline OER and HER Bi-functional Electrocatalyst Applications. *J. Alloys Compd.* **2021**, *858*, No. 157679.

(44) Khan, I. A.; Badshah, A.; Nadeem, M. A.; Haider, N.; Nadeem, M. A. A Copper Based Metal-organic Framework as Single Source for the Synthesis of Electrode Materials for High-performance Supercapacitors and Glucose Sensing Applications. *Int. J. Hydrogen Energy* **2014**, *39*, 19609–19620.

(45) Zhang, Z.; Yu, J.; Zhang, J.; Ge, Q.; Xu, H.; Dallmann, F.; Dittmeyer, R.; Sun, J. Tailored Metastable Ce-Zr Oxides with Highly Distorted Lattice Oxygen for Accelerating Redox Cycles. *Chem. Sci.* **2018**, *9*, 3386–3394.

Recommended by ACS

Highly Cyclic Stability and Absorbent Activity of Carbide Slag Doped with MgO and ZnO for Thermochemical Energy Storage

Caiyun Gao, Mei Li, *et al.*

DECEMBER 02, 2022

ACS OMEGA

READ 

Magnesium Cobaltite Embedded in Corncob-Derived Nitrogen-Doped Carbon as a Cathode Catalyst for Power Generation in Microbial Fuel Cells

Simran Kaur Dhillon and Patit Paban Kundu

OCTOBER 12, 2022

ACS APPLIED MATERIALS & INTERFACES

READ 

$\text{Mg}_2\text{Fe}_2\text{O}_5$ Nanoparticle-Decorated $\text{Ca}_2\text{Fe}_2\text{O}_5$ - CaFe_2O_4 Heterostructure for Efficient Photocatalytic CO_2 Conversion

You-Hao Chang, Jih-Jen Wu, *et al.*

SEPTEMBER 12, 2022

ACS SUSTAINABLE CHEMISTRY & ENGINEERING

READ 

Facile Synthesis of MgO Nanoparticle-Embedded Fe/N/S Codoped Carbon Materials from Oily Sludge for Efficient CO_2 Capture

Wu-Jun Liu, Yu Xu, *et al.*

JUNE 09, 2022

ACS ES&T ENGINEERING

READ 

Get More Suggestions >